Enhanced Nanoparticle Rejection in Aligned Boron Nitride Nanotube Membranes

Serena Casanova,[†] *Sritay Mistry,*[‡] *Saeed Mazinani, Matthew K. Borg,*[‡] *Y. M. John Chew, and Davide Mattia*[†1]

[†]Department of Chemical Engineering, Centre for Advanced Separations Engineering, University of Bath, BA27AY, UK

[‡]School of Engineering, University of Edinburgh, EH9 3FB, UK

Supporting Information

Contents
No table of contents entries found.

S1. Membranes Synthesis Methods

Boron nitride (BN) was deposited in the pores of anodic alumina membranes (AAMs) via non-catalytic chemical vapour deposition (CVD), producing boron nitride nanotube membranes (BNNT-AAMs). 13 mm diameter, thermally treated, symmetric AAMs templates were purchased from InRedox, with pore diameters ranging from ~10 nm to ~30 nm. The membranes were assembled in a custom-made quartz membrane holder (Fig.S1a) inside a quartz tube (ID 20 mm, OD 22 mm) to be inserted in the centre of a horizontal TZF 12/38/850 type CARBOLITE furnace (Figure S1b).

---

[1] Corresponding author email: d.mattia@bath.ac.uk

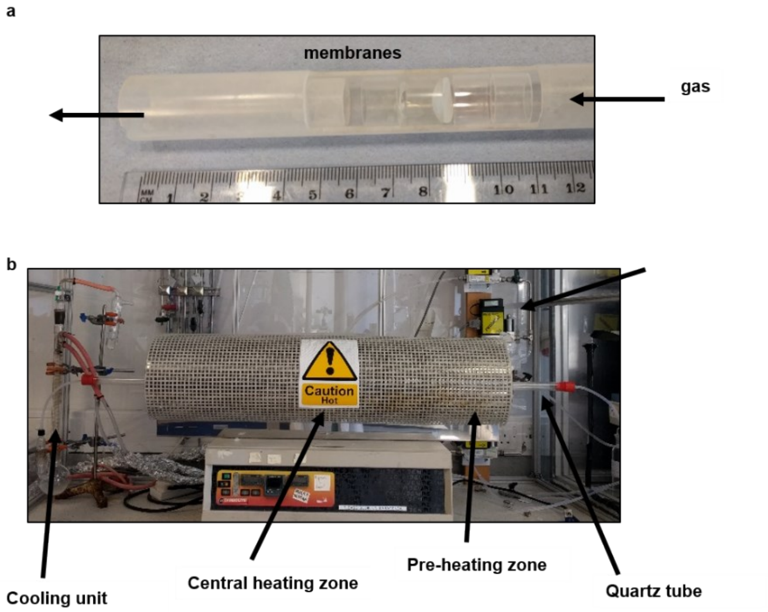

Figure S 1 (a) Customised quartz membrane holder and **(b)** furnace setup where the gas is controlled by mass flow controllers, enters the quartz tube from the right hand side and is cooled at the outlet in a water cooled unit. The borazane precursor is preheated in a pre-heating zone where it degrades in polyiminoborane, $B_3H_6N_3$ and hydrogen.

Gas flows to the furnace were controlled using Omega FMAb5400A/5500A mass flow controllers (MFCs) regulated by a LabVIEW program. Once the quartz tube was sealed, the temperature was ramped up at 10 ºC/min under 150 sccm Ar flow to displace residual air left in the reactor. The precursor (borazane ≥ 97% purity, Sigma Aldrich) was sublimated at 80-100 ºC in the reactor pre-heating zone. The synthesis was then carried out for 40 min under a 15:135 sccm H_2:Ar flow with Reynolds number ~ 1 at the synthesis temperature of 1000 ºC. The gas carried along the products of the degradation of borazane, namely polyiminoborane, borazine and hydrogen [1]. Borazine degraded into BN and hydrogen at 1000 ºC in the central section of the furnace, forming a BN layer onto the AAMs. After synthesis, the BNNTs membranes were left to cool down to room temperature and were gently rinsed with deionised (DI) water to remove any debris.

As demonstrated in Figure S 2, not all anodic alumina membranes are suitable for the synthesis of BNNTs. Since the synthesis happens in a reducing environment due to the presence of hydrogen gas, it is not advisable to choose alumina templates containing residual oxalic groups from the anodization process [2], as this might result in carbon impurities retained as carbonate or carboxyl groups after synthesis.

Figure S 2 Anodic alumina result of a synthesis process on a membrane anodised with oxalic acid as electrolyte.

S.2 Characterisation Methods

Table S 1 Size, pH, colloids zeta potential (ζ_c) and ionic strength (I) of the nanoparticles used in this work. The particle diameter (D_{NP}) is computed form statistical analysis of TEM micrographs in Fig.s S3 and S4

Nanoparticle	Supplier	D_{NP} (nm)	pH	ζ_c (mV)	I (mol L^{-1})
S1	Sigma Aldrich	9.2 ± 1.8	9.2	- 12.7 ± 0.6	2.18×10^{-2}
S2	Sigma Aldrich	14.7 ± 1.8	8.6	- 27.4 ± 1.9	2.18×10^{-2}
S3	Fisher Scientific	19.2 ± 2.6	5.5	- 18.5 ± 1.9	2.18×10^{-2}
S4	Sigma Aldrich	27.1 ± 3.2	8.8	- 37.6 ± 4.1	2.18×10^{-2}
H1	BASF	15.8 ± 2.2	4.9	8.6 ± 1.5	6.30×10^{-6}
H2	BASF	17.2 ± 2.2	5.3	3.8 ± 1.6	2.51×10^{-6}
H3	Sigma Aldrich	37.3 ± 4.2	6.0	19.9 ± 0.2	5.05×10^{-7}

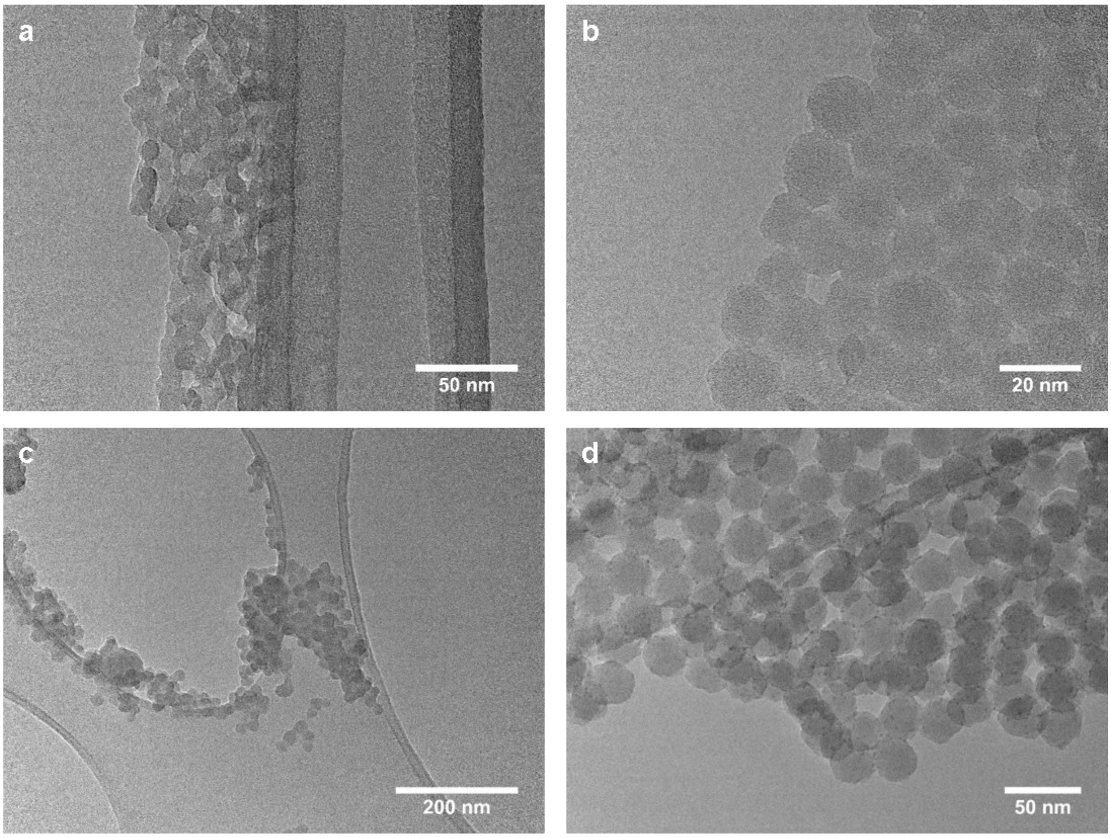

Figure S 3 TEM micrographs of silica nanoparticles on Lacey carbon **(a)** S1, **(b)** S2, **(c)** S3 and **(d)** S4.

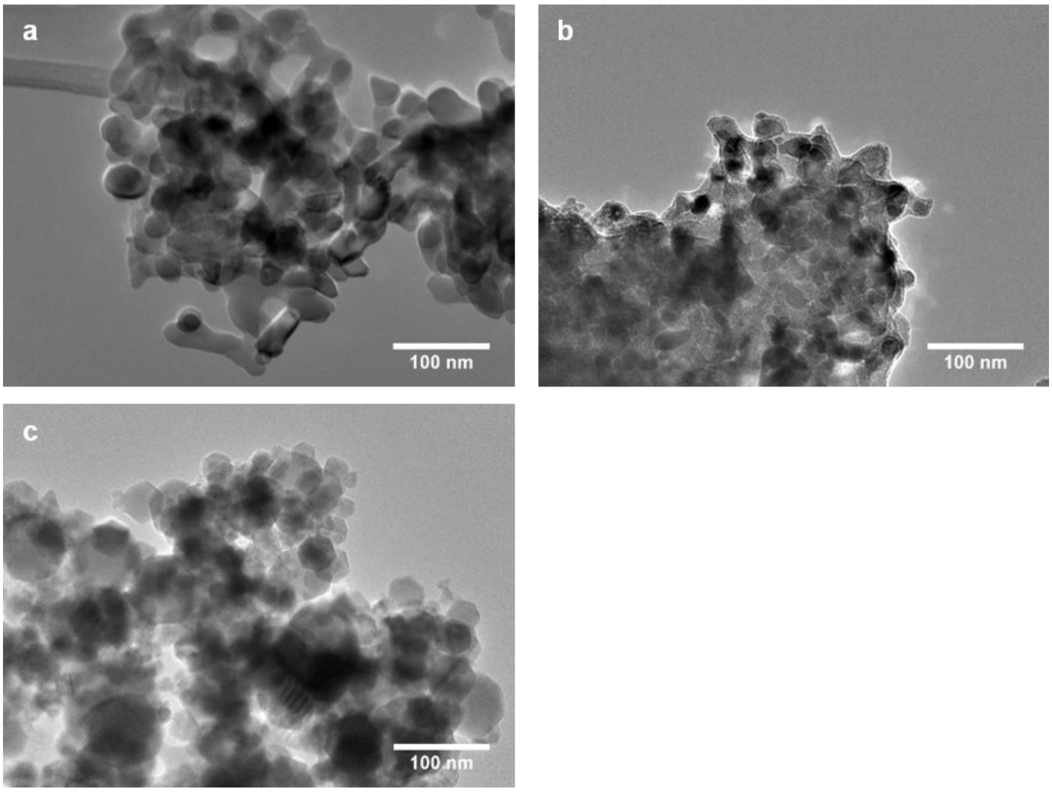

Figure S 4 TEM micrographs of hematite nanoparticles on Lacey carbon **(a)** H1, **(b)** H2 and **(e)** H3.

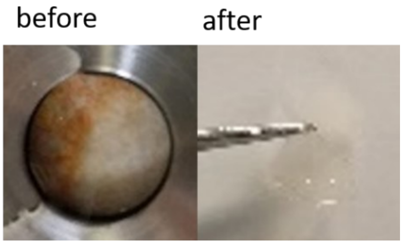

Figure S 5 Image of the membrane before and after backflushing.

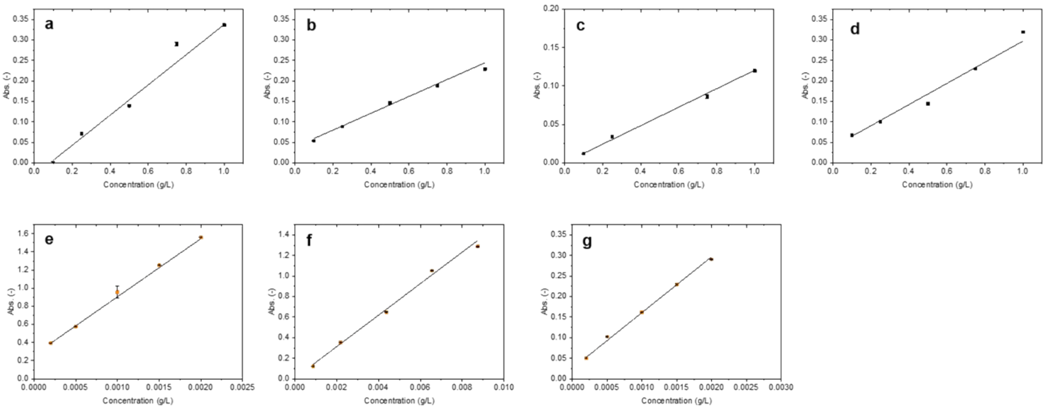

Figure S 6 UV-vis calibration curves for **(a)** S1, **(b)** S2, **(c)** S3, **(d)** S4, **(e)** H1, **(f)** H2 and **(g)** H3. The acquisition time for each datapoint is 0.1 sec, and 3 repeats are performed for each concentration.

An Agilent UV-vis Cary 100 setup was used to relate the concentration of nanoparticles in the water suspension to absorbance in the spectral region between 190 and 900 nm. UV-vis calibration curves (Figure S 6) were prepared by diluting a starting suspension at the highest concentration five times. Predictions using the prepared calibration curve were associated to errors so calculated [7]:

$$s_{X0} = \frac{s(r)}{m}\sqrt{\frac{1}{N}+\frac{1}{n}+\frac{(\bar{y}_0-\bar{y})^2}{m^2\sum_{i=1}^{n}(x_i-\bar{x})^2}}, \tag{S1}$$

where $s(r) = \sqrt{\sum_{i=1}^{n}(y_i-\hat{y}_i)^2 \Big/ (n/2)}$ is the residual standard deviation with y_i as the observed value of absorbance for a given concentration value of x_i; $\hat{y}_i$ is the value of absorbance predicted by the plotted calibration line (with gradient m) for a given value of concentration x_i, and n is the number of paired calibration points; N is the number of repeat measurements made on the sample, which was three in all the samples collected; $\bar{y}_0$ is the mean of N repeat measurements of absorbance for the sample, while $\bar{y}$ is the mean of the absorbance values for the calibration standards; $\bar{x}$ is the mean of the concentration values [8]. Hellma quartz glass 1400 µl cuvettes with 10 mm optical path length were used for the UV-vis testing of all the standards and samples.

S.3 Static Adsorption Tests Methods

Static adsorption tests were performed in 20 ml glass vials containing an alumina disc or a BN coated alumina disc dipped in the nanoparticle suspension, with a control vial containing only the nanoparticle suspension. The solutions were gently shaken with an IKA KS 130 for 24 h at a temperature of 25 °C and with stirring at 80 rpm. The vials were capped to minimise evaporation. The supernatant of each test vial was then collected. The concentration of silica and hematite in the solutions was analysed by UV–Vis spectrophotometry. The concentration of nanoparticles in the vials containing alumina or BN-coated alumina is referred to as C_S, while the concentration of nanoparticles in the control vial containing the solution only is referred to as C_C. The adsorption $A(\%)$ of nanoparticles on membranes and gaskets was then calculated by:

$$A(\%) = \left(1-\frac{C_S}{C_C}\right) \times 100. \tag{S2}$$

S.4 Numerical simulations

The conservation of mass and momentum equations, and particle tracing model for steady state and laminar flow conditions were solved by using a commercial CFD software COMSOL Multiphysics^{TM} v5.4. In all the numerical models presented in this study, the flowing fluid was assumed to be Newtonian and incompressible. The overall domain size was 40 nm × 84 mnm (height × length). The domain was discretised into 8112 unstructured triangular elements, respectively, using finite element method. For the computation of isoforce lines, the domain was considered symmetrical for x=42 nm.

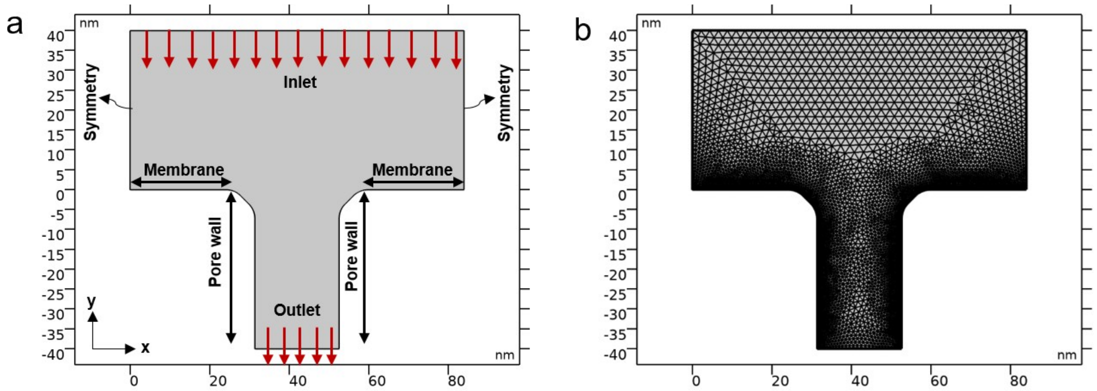

Figure S 7 (a) Geometry and **(b)** mesh discretisations used in the simulations.

S.5 CFD Governing Equations and Boundary Conditions

Continuous phase

The continuous phase was assumed to be water with density, ρ = 1000 kg m^{-3} and dynamic viscosity, μ = 0.001 kg m^{-1} s^{-1}. The hydrodynamics was modelled by solving the continuity and Navier-Stokes equations:

Continuity: $\nabla \cdot u = 0$ (S3)

Navier-Stokes: $\rho\ (u \cdot \nabla u) =- \ \nabla p + \mu \nabla^2 u$ (S4)

where u is the velocity (u,v,w) and p is the pressure. The boundary conditions were:

i. *Inlet*: Pressure i.e. when $y =$ 40 nm, $0 < x < 84$ nm.
ii. *Left wall*: Symmetry i.e. when $x =$ 0 nm, $0 < y < 40$ nm; $u = 0$.
iii. *Right wall*: Symmetry i.e. when $x =$ 84 nm, $0 < y < 40$ nm; $u = 0$.
iv. *Membrane*: No-slip and impermeable i.e. when $y =$ 0 nm, $0 < x < 26$ nm and $58 < x < 84$ nm.
v. *Pore wall*: No-slip and impermeable i.e. when $0 < y < 40$ nm, $26 < x < 31$ nm and $53 < x < 58$ nm.
vi. *Outlet*: Normal outflow velocity i.e. when $y =$ 40 nm, $31 < x < 53$ nm. The outlet velocity was obtained by dividing the experimental flow through the membrane by the number of pores at the designated pressure.

Particles

The particle was assumed to be spherical with density, ρ_p = 2650 kg m^{-3}, and diameter, D_{NP} = 19.2 nm from the experimental value for particle S3. It was further assumed that there were no particle-particle interactions. The boundary conditions were:

i. *Inlet*: Four particles were randomly released at the inlet between 0 s and 10^{-4} s with time interval 10^{-7} s.
ii. *Left wall*: Impermeable, the particles were set to bounce off when they contact the wall.
iii. *Right wall*: Impermeable, the particles were set to bounce off when they contact the wall.
iv. *Membrane*: Impermeable, the particles were set to bounce off when they contact the wall.
v. *Pore wall*: Impermeable, the particles were set to bounce off when they contact the wall.
vi. *Outlet*: The particles were set to freeze once they exit through the outlet.

Sieving and fouling are governed by the interplay of forces acting on feed particles [11]. Drag (F_D), electrostatic (F_E) and Brownian (F_B) are reputed as the primary non negligible forces that should be analysed when pollutants size is comparable to membrane pore size [12]. It is possible to study the combined effect of such forces on particle trajectories in dead end filtration by numerically integrating the Langevin equation [13], used to describe the stochastic motion of a particle subject to forces:

$$m_p \frac{du_p}{dt} = F_D + F_E + F_B \tag{S5}$$

In Eq. 13, the term u_p is the particle velocity vector and m_p its mass, obtained in the model assuming a perfectly spherical particle with density ρ_p. The drag force arises from the friction induced by the relative velocity of the colloid and fluid medium and is so expressed:

$$F_D = 3\pi\mu D_{NP}[K_p u_p - K_f u_f] \tag{S6}$$

The designation u_f represents the unperturbated fluid velocity evaluated in absence of the particle, D_{NP} is the particle diameter, μ the fluid viscosity, K_p and K_f hydrodynamic factors accounting for the hydrodynamic hindrance due to interactions between the particle and membrane surface.

An expression for F_E based on DLVO (Derjaguin, Landau, Verwey, and Overbeek) theory was introduced by Bowen et al. [14] as a function of the surface zeta potential of the particle (ζ_c) and membrane (ζ_m). F_E is dependent on the distance h between the particle centre and the membrane and the Debye length ($\lambda_D = 1/\kappa = 3.07\ \times\ 10^{-10}/\sqrt{I}$):

$$F_E = \frac{2\pi\kappa\varepsilon_r\varepsilon_0}{g}\left[\frac{2\zeta_c\zeta_m e^{\kappa\left[h - \left(\frac{D_{NP}}{2}\right)\right]} - (\zeta_m^2 + \zeta_c^2)}{e^{2\kappa\left[h - \left(\frac{D_{NP}}{2}\right)\right]} - 1}\right], \tag{S7}$$

where ε_0 is the vacuum permittivity, ε_r is the dielectric constant and g is a steric factor depending on h linked to the specific geometry of the system [12]. Values for ζ_c and ζ_m were entered from experimental values at pH 6.

Ultimately, the Brownian force is modelled on the basis of the Gaussian white noise method [15]:

$$F_B = \iota\sqrt{\frac{6\pi\mu D_{NP} k_B T}{\Delta t}} \tag{S8}$$

where ι is a randomly generated number, Δt is a predetermined time-step set to 10^{-7} s in all simulations.

S.6 Membranes Characterisation Results

FESEM analysis of the BNNT-AAMs showed a clean surface with open pores after synthesis (Figure S 8a), and EDX scans revealed the uniform deposition of B and N on the AAM (Figure S 8b). The deposition of BN on Al_2O_3 is reported in these scans with atomic ratios around 50% higher than the theoretical value (B/N atomic ratio of 1).

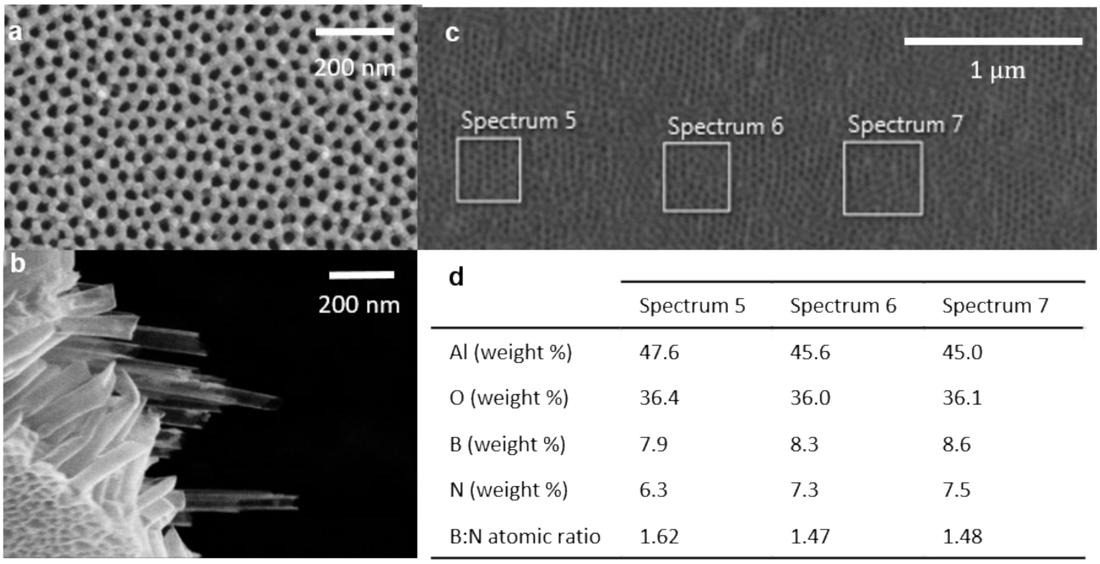

	Spectrum 5	Spectrum 6	Spectrum 7
Al (weight %)	47.6	45.6	45.0
O (weight %)	36.4	36.0	36.1
B (weight %)	7.9	8.3	8.6
N (weight %)	6.3	7.3	7.5
B:N atomic ratio	1.62	1.47	1.48

Figure S 8 **(a)** Surface of a BNNT-AAMs after synthesis and **(b)** nanotubes released from a cracked CNTs membrane. **(c)** EDX spectrum of an area on the membrane's surface, with **(d)** some examples spectra results showing a 1.62 (Spectrum 5), 1.47 (Spectrum 6) and 1.48 (Spectrum 7) B:N atomic ratio (details in Table S 2).

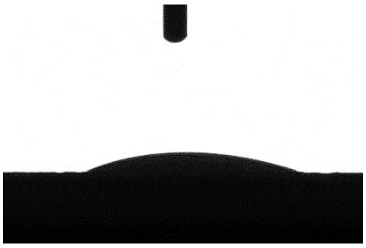

Figure S 9 Uncoated alumina surfaces present a much more hydrophilic nature [17, 21] than BN-coated discs.

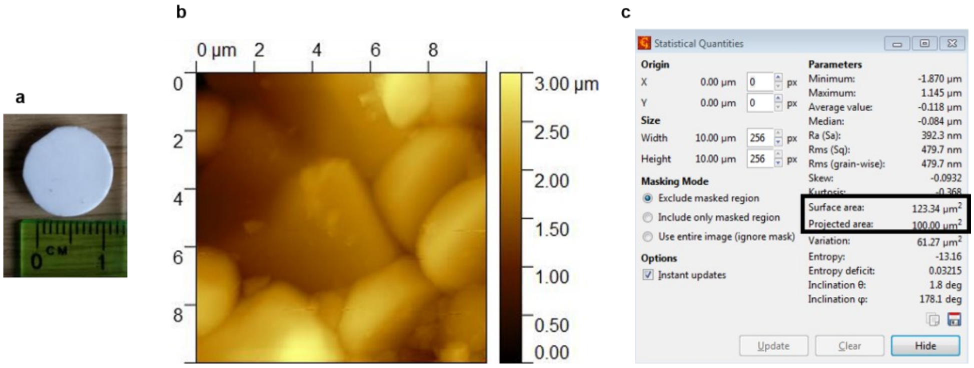

Origin
X 0.00 µm 0 px
Y 0.00 µm 0 px
Size
Width 10.00 µm 256 px
Height 10.00 µm 256 px
Masking Mode
● Exclude masked region
○ Include only masked region
○ Use entire image (ignore mask)
Options
☑ Instant updates

Parameters
Minimum: -1.870 µm
Maximum: 1.145 µm
Average value: -0.118 µm
Median: -0.084 µm
Ra (Sa): 392.3 nm
Rms (Sq): 479.7 nm
Rms (grain-wise): 479.7 nm
Skew: -0.0932
Kurtosis: -0.368
Surface area: 123.34 µm²
Projected area: 100.00 µm²
Variation: 61.27 µm²
Entropy: -13.16
Entropy deficit: 0.03215
Inclination θ: 1.8 deg
Inclination φ: 178.1 deg

Figure S 10 **(a)** Alumina substrate used for BN contact angle measurements, **(b)** AFM used for roughness determination and correspondent **(c)** statistical analysis output showing the quantities used for the determination of the parameter r in Eq. (S3).

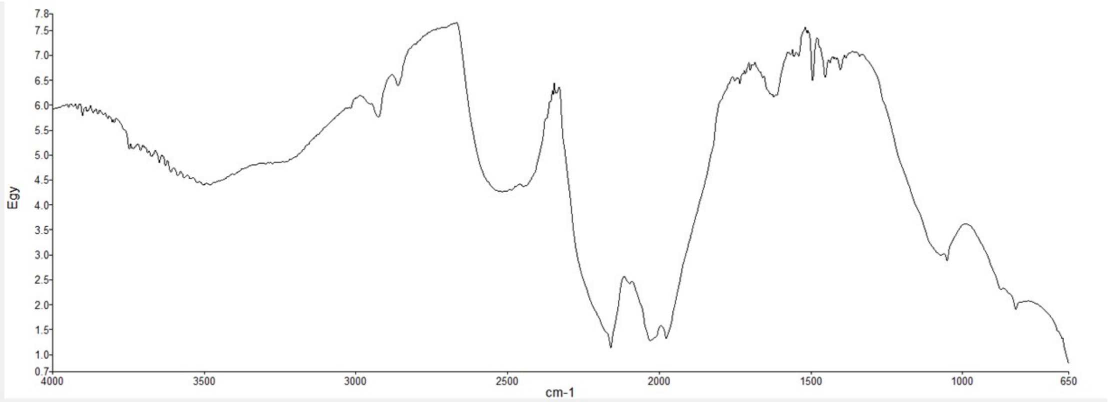

Figure S 11 FTIR machine background.

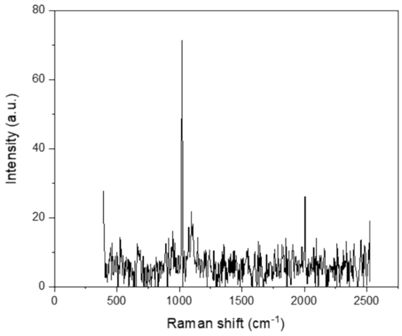

Figure S 12 Raman blank spectrum (i.e. without sample) that was subtracted to the spectra presented in this work.

S.7 Experimental Membrane Performance

Pure water tests are performed at different transmembrane pressures, as reported in Table S 4 In the ceramic membranes studied deformation of the matrix does not take place during testing [10].

Table S 2 Transmembrane pressures applied to each sample during pure flow tests.

Name	D **(nm)**	ΔP_1 **(bar)**	ΔP_2 **(bar)**	ΔP_3 **(bar)**	ΔP_4 **(bar)**
SC_263	17.76 ± 3.89	3.79 ± 0.05	4.10 ± 0.05	4.64 ± 0.05	4.77 ± 0.05
SC_268	19.78 ± 4.76	0.67 ± 0.05	1.89 ± 0.05	2.36 ± 0.05	2.72 ± 0.05
SC_274	19.00 ± 2.06	0.84 ± 0.05	1.23 ± 0.05	-	-
SC_275	28.85 ± 3.75	3.01 ± 0.05	3.27 ± 0.05	3.57 ± 0.05	-
SC_283	22.53 ± 3.66	1.44 ± 0.05	2.33 ± 0.05	3.05 ± 0.05	-
SC_285	23.21 ± 3.08	0.73 ± 0.05	1.20 ± 0.05	2.33 ± 0.05	4.34 ± 0.05
SC_293	22.61 ± 3.28	0.65 ± 0.05	0.98 ± 0.05	1.06 ± 0.05	1.14 ± 0.05

SC_294	19.77 ± 4.16	0.65 ± 0.05	1.00 ± 0.05	1.07 ± 0.05	1.12 ± 0.05
SC_295	23.90 ± 3.62	4.28 ± 0.05	5.65 ± 0.05	7.03 ± 0.05	-
SC_297	28.89 ± 4.11	0.65 ± 0.05	0.98 ± 0.05	1.06 ± 0.05	1.14 ± 0.05
SC_298	21.73 ± 4.62	2.82 ± 0.05	4.57 ± 0.05	5.67 ± 0.05	6.56 ± 0.05
SC_313	19.53 ± 6.1	5.46 ± 0.05	5.48 ± 0.05	-	-
SC_314	25.67 ± 2.74	0.65 ± 0.05	0.82 ± 0.05	1.06 ± 0.05	-
SC_315	28.60 ± 2.22	0.49 ± 0.05	0.64 ± 0.05	0.83 ± 0.05	-
SC_316	21.31 ± 3.78	0.33 ± 0.05	0.53 ± 0.05	0.73 ± 0.05	0.91 ± 0.05
SC_317	21.32 ± 3.69	0.27 ± 0.05	0.44 ± 0.05	0.60 ± 0.05	0.91 ± 0.05
SC_319	27.71 ± 3.91	0.39 ± 0.05	0.71 ± 0.05	0.90 ± 0.05	-
SC_329	21.41 ± 3.92	0.93 ± 0.05	1.21 ± 0.05	1.39 ± 0.05	-
SC_330	27.32 ± 3.86	0.74 ± 0.05	0.98 ± 0.05	1.25 ± 0.05	-
SC_345	22.61 ± 4.68	0.96 ± 0.05	1.20 ± 0.05	-	-

Table S 3 Raw data for pure water flow tests.

Name	D **(nm)**	K **(L m^{-2} h^{-1} bar^{-1})**	ϕ	μ_B **(Pa s)**	L **(m)**	ε **(-)**	A_{mem} **(m^2)**
SC_263	17.76 ± 3.89	2.91 ± 0.39	0.04	0.00105	5E-05	1.1	7.9E-05
SC_268	19.78 ± 4.76	5.46 ± 0.58	0.08	0.00114	5E-05	1.1	7.9E-05
SC_274	19.00 ± 2.06	33.52 ± 5.81	0.12	0.00111	5E-05	3.7	7.9E-05
SC_275	28.85 ± 3.75	36.03 ± 3.91	0.20	0.00111	5E-05	1.1	7.9E-05
SC_283	22.53 ± 3.66	20.21 ± 3	0.10	0.00105	5E-05	1.9	7.9E-05
SC_285	23.21 ± 3.08	21.27 ± 5.2	0.11	0.00103	5E-05	1.6	7.9E-05
SC_293	22.61 ± 3.28	18.88 ± 2.62	0.19	0.00103	5E-05	0.7	7.9E-05
SC_294	19.77 ± 4.16	22.04 ± 7.04	0.07	0.00111	5E-05	4.0	7.9E-05
SC_295	23.90 ± 3.62	4.77 ± 1.11	0.11	0.00103	5E-05	0.4	7.9E-05
SC_297	28.89 ± 4.11	24.8 ± 5.06	0.19	0.00105	5E-05	0.7	7.9E-05
SC_298	21.73 ± 4.62	5.15 ± 0.7	0.11	0.00100	5E-05	0.4	7.9E-05
SC_313	19.53 ± 6.1	14.54 ± 0.07	0.12	0.00098	5E-05	1.4	1.3E-05
SC_314	25.67 ± 2.74	6.32 ± 0.46	0.17	0.00103	5E-05	0.3	7.9E-05
SC_315	28.60 ± 2.22	6.77 ± 2.2	0.19	0.00103	5E-05	0.2	7.9E-05
SC_316	21.31 ± 3.78	7.1 ± 1.77	0.11	0.00100	5E-05	0.6	7.9E-05
SC_317	21.32 ± 3.69	8.07 ± 1.15	0.12	0.00100	5E-05	0.7	7.9E-05
SC_319	27.71 ± 3.91	8.16 ± 0.84	0.22	0.00111	5E-05	0.2	7.9E-05
SC_329	21.41 ± 3.92	4.38 ± 0.85	0.10	0.00111	5E-05	0.5	7.9E-05
SC_330	27.32 ± 3.86	4.2 ± 0.71	0.18	0.00111	5E-05	0.2	7.9E-05
SC_345	22.61 ± 4.68	22.79 ± 1.94	0.19	0.00111	5E-05	1.2	2.0E-5

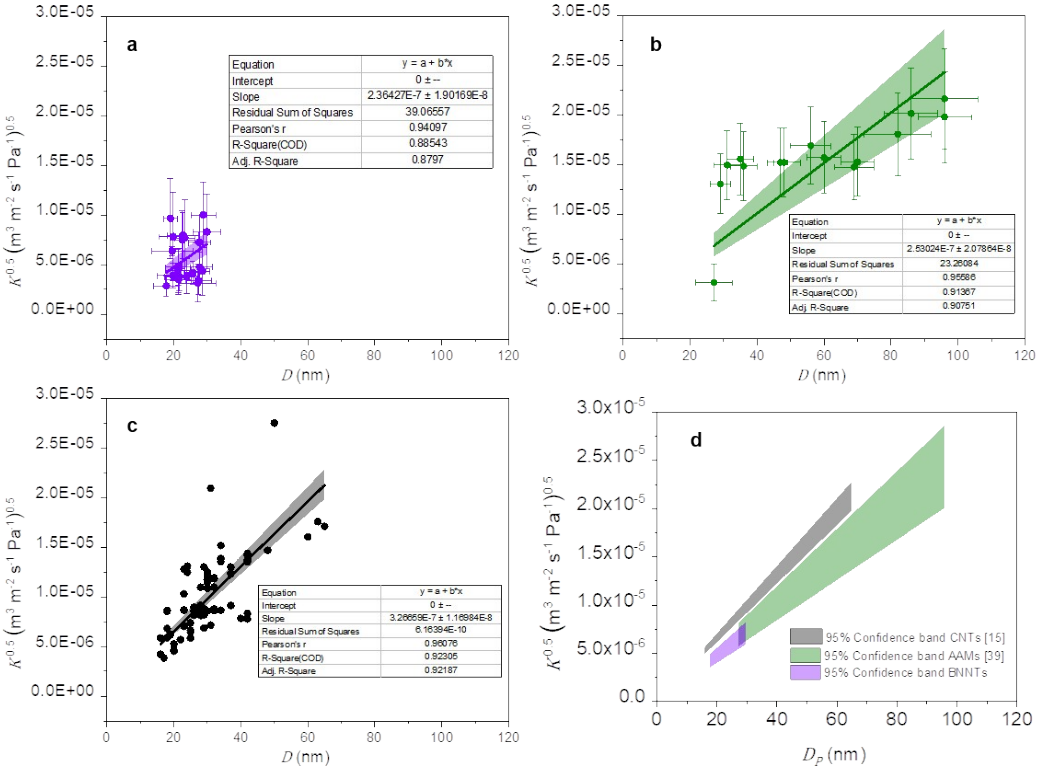

Figure S 13 Linear fitting regressions for **(a)** BNNTs in this work, **(b)** AAMs [18] and **(c)** CNTs [3]. The inset tables report Pearson's r (a measure the strength of linear relationship between paired data), R^2 (a statistical measure of the linear regression) and Adj. R^2 (a modified version of R^2, adjusted for the number of predictor in the fitted line). Permeance 95 % confidence bands of regression on a set of BNNT-AAMs with D_P ranging from 17.8 to 28.9 nm are presented with the associated measurement error, and compared to the linear fitting of literature data for bare alumina [18] and CNTs [3] membrane. The raw data for this graph and regression results of the model used can be found in Table S 3.

The source of error on the calculation of the average diameter in Figure S 13 is given by the measured nanotube size distribution, which in turn depends on the alumina template pore size distribution and FESEM resolution. Results for membranes that suffered obvious cracks during handling are not reported in this work, but pinholes or non-evident pore clogging could be the source of errors in permeance recorded during the measurements.
The pure water permeance in BNNTs membranes ranged from ~3 LMH/bar for the smallest pore size to ~25 LMH/bar for the biggest pore size (Figure S 13), values comparable to those of commercial membranes.[3]

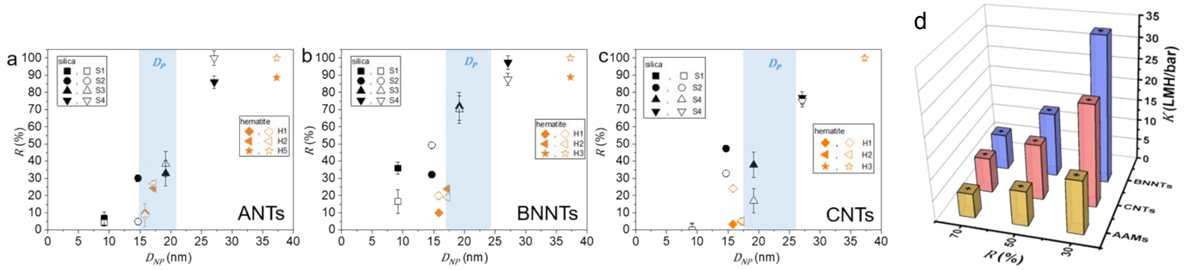

Figure S 14 Rejection R reported as a function of the diameter of the particle tested D_{NP} on **(a)** two ANTs membranes (av. pore diameter 18 ± 3 nm for both); **(b)** two BNNT membranes (av. pore diameter 22.2 ± 2.2 nm in the first test (filled symbols, black for silica and orange for hematite) and 20.2 ± 2.9 nm in the second test (empty symbols, black for silica and orange for hematite) and **(c)** two CNTs membranes (av. pore diameter 21.1 ± 3.6 nm in the first test (filled symbols, black for silica and orange for hematite) and 24.1 ± 2.3 nm in the second test (empty symbols, black for silica and orange for hematite). The average pore diameter (D_P) is indicated by a blue band on the graph. The larger diameter of BNNTs and CNTs compared to AAM is due to the different type of anodic alumina templates used for each synthesis. All rejection data is reported in Table S 4.

Table S 4 Rejection data for the alumina membranes tested. Operating pressure is 1 bar.

AAM 1 (D_P=18.0±3.0)							
Particle	**D (nm)**	**Err D (nm)**	**Cf (g/L)**	**Cp (g/L)**	**xs0 (g/L)**	**Ave Rejection**	**Err Rejection**
S1	9.20	1.82	1.00	0.93	0.04	6.77	3.94
				0.93	0.04		
				0.93	0.04		
S4	27.10	3.21	1.00	0.14	0.04	85.98	3.63
				0.14	0.04		
				0.14	0.04		
S3	19.20	2.60	1.00	0.67	0.07	32.99	7.38
				0.67	0.07		
				0.67	0.07		
S2	14.70	1.80	1.00	0.70	0.02	30.15	1.99
				0.70	0.02		
				0.70	0.02		
H2	17.24	2.22	0.00875	0.00662	0.00016	24.31	1.82
				0.00662	0.00016		
				0.00662	0.00016		
H1	15.83	2.19	0.002	0.0018	0.0000	9.68	2.03
				0.0018	0.0000		
				0.0018	0.0000		
H3	37.26	4.20	0.002	0.00000	0.00003	100.00	1.42
				0.00000	0.00003		

				0.00000	0.00003		
AAM 2 (D_P=18±3)							
Particle	**D (nm)**	**Err D (nm)**	**Cf (g/L)**	**Cp (g/L)**	**xs0 (g/L)**	**Ave Rejection**	**Err Rejection**
S1	9.20	1.82	1.00	0.96	0.04	4.29	1.99
				0.96	0.04		
				0.96	0.04		
S4	27.10	3.21	1.00	0.00	0.04	100.00	4.17
				0.00	0.04		
				0.00	0.04		
S3	19.20	2.60	1.00	0.62	0.07	38.31	7.48
				0.62	0.07		
				0.62	0.07		
S2	14.70	1.80	1.00	0.95	0.02	4.98	1.95
				0.95	0.02		
				0.95	0.02		
H2	17.24	2.22	0.00875	0.00640	0.00016	26.91	1.80
				0.00640	0.00016		
				0.00640	0.00016		
H1	15.83	2.19	0.0006	0.0005	0.0000	8.63	6.77
				0.0005	0.0000		
				0.0005	0.0000		
H3	37.26	4.20	0.002	0.00023	0.00003	88.59	1.28
				0.00023	0.00003		
				0.00023	0.00003		

Table S 5 Rejection data for the BNNTs membranes tested. Operating pressure is 1 bar.

BN-AAM 1 (D_P=22.2±2.2)							
Particle	**D (nm)**	**Err D (nm)**	**Cf (g/L)**	**Cp (g/L)**	**sx0 (g/L)**	**Ave Rejection**	**Err Rejection**
S1	9.20	1.82	1.00	0.64	0.04	36.00	3.55
				0.64	0.04		

				0.64	0.04		
S4	27.10	3.21	1.00	0.03	0.04	97.36	3.85
				0.03	0.04		
				0.03	0.04		
S3	19.20	2.60	1.00	0.28	0.08	72.00	8.11
				0.28	0.08		
				0.28	0.08		
S2	14.70	1.80	1.00	0.68	0.02	32.20	1.98
				0.68	0.02		
				0.68	0.02		
H2	17.24	2.22	0.00875	0.00666	0.00016	23.93	1.82
				0.00666	0.00016		
				0.00666	0.00016		
H1	15.83	2.19	0.002	0.002	0.000	10.0	2.01
				0.002	0.000		
				0.002	0.000		
H3	37.26	4.20	0.002	0.000	0.000	100.00	1.42
				0.000	0.000		
				0.000	0.000		
BN-AAM 2 (D_P=20.2±2.9)							
Particle	**D (nm)**	**Err D (nm)**	**Cf (g/L)**	**Cp (g/L)**	**sx0 (g/L)**	**Ave Rejection**	**Err Rejection**
S1	9.20	1.82	0.52	0.43	0.04	16.62	6.83
				0.43	0.04		
				0.43	0.04		
S4	27.10	3.21	1.00	0.12	0.04	87.68	3.55
				0.12	0.04		
				0.12	0.04		
S3	19.20	2.60	1.00	0.30	0.08	70.01	8.07
				0.30	0.08		
				0.30	0.08		
S2	14.70	1.80	1.00	0.51	0.02	49.32	1.95
				0.51	0.02		
				0.51	0.02		
H2	17.24	2.22	0.00875	0.00708	0.00016	19.05	1.85
				0.00708	0.00016		
				0.00708	0.00016		
H1	15.83	2.19	0.002	0.002	0.000	19.91	1.94
				0.002	0.000		
				0.002	0.000		
H3	37.26	4.20	0.002	0.000	0.000	88.83	1.28
				0.000	0.000		
				0.000	0.000		

Table S 6 Rejection data for the CNTs membranes tested. Operating pressure is 1 bar.

CNTs-AAM 1 (D_P=21.1±3.6)

Particle	**D (nm)**	**Err D (nm)**	**Cf (g/L)**	**Cp (g/L)**	**sx0 (g/L)**	**Ave Rejection**	**Err Rejection**
S1	9.20	1.82	1.00	1.00	0.04	0.00	3.55
				1.00	0.04		
				1.00	0.04		
S4	27.10	3.21	1.00	0.23	0.03	76.99	3.49
				0.23	0.03		
				0.23	0.03		
S3	19.20	2.60	1.00	0.62	0.07	37.94	7.48
				0.62	0.07		
				0.62	0.07		
S2	14.70	1.80	1.00	0.53	0.02	47.39	1.90
				0.53	0.02		
				0.53	0.02		
H2	17.24	2.22	0.00875	0.00834	0.00017	4.73	1.98
				0.0834	0.00017		
				0.0834	0.00017		
H1	15.83	2.19	0.002	0.00193	0.00004	3.30	2.10
				0.00193	0.00004		
				0.00193	0.00004		
H3	37.26	4.20	0.002	0.00000	0.00002		
				0.00000	0.00002		
				0.00000	0.00002		

CNTs-AAM 2 (D_P=24.1±2.3)

Particle	**D (nm)**	**Err D (nm)**	**Cf (g/L)**	**Cp (g/L)**	**sx0 (g/L)**	**Ave Rejection**	**Err Rejection**
S1	9.20	1.82	1.00	1.00	0.04	0.00	4.19
				1.00	0.04		
				1.00	0.04		
S4	27.10	3.21	1.00	0.25	0.03	74.89	3.46
				0.25	0.03		
				0.25	0.03		
S3	19.20	2.60	1.00	0.83	0.07	17.00	7.00
				0.83	0.07		
				0.83	0.07		
S2	14.70	1.80	1.00	0.67	0.02	33.00	2.00
				0.67	0.02		
				0.67	0.02		
H2	17.24	2.22	0.00875	0.00829	0.00017	5.24	1.97
				0.00829	0.00017		
				0.00829	0.00017		
H1	15.83	2.19	0.002	0.00152	0.00004	24.07	1.91
				0.00152	0.00004		
				0.00152	0.00004		
H3	37.26	4.20	0.002	0.00000	0.00003		

				0.00000	0.00003	100.00	1.59
				0.00000	0.00003		

Table S 7 Data on average rejection used to normalise rejection data for a set nanotube diameter. R^2 values for the linear fitting of BNNTs, CNTs and AAMs on alumina are, respectively: R^2=0.9687, R^2=0.8419 and R^2=0.9359.

		Alumina	**Cured Carbon**	**Boron Nitride**	**Alumina**	**Carbon Cured**	**Boron Nitride**
Average Dp		18	21.2	22.6	18	21.2	22.6
SILICA							
Particle	**D (nm)**	**Average Rejection**			**Normalised Rejection**		
S1	9.20	5.53	0.00	26.31	0.31	0.00	1.22
S4	27.10	92.99	75.94	92.52	5.17	3.38	4.36
S3	19.20	35.65	27.47	71.01	1.98	1.25	3.35
S2	14.70	17.56	40.20	40.76	0.98	1.81	1.95
HEMATITE							
Particle	**D (nm)**	**Average Rejection**			**Normalised Rejection**		
H1	17.24	25.61	4.99	21.49	1.42	0.22	1.01
H2	15.83	9.16	13.69	15.81	0.51	0.58	0.76
H3	37.26	94.29	100.00	94.41	5.24	4.44	4.45

		Alumina	Cured Carbon	Boron Nitride	Alumina	Carbon Cured	Boron Nitride
Average Dp		18	21.2	22.6	18	21.2	22.6
SILICA							
Particle	D (nm)	**Normalised Particle D**			**Normalised Particle D**		
S1	9.20	0.51	0.43	0.41	0.51	0.43	0.41
S4	27.10	1.51	1.28	1.20	1.51	1.28	1.20
S3	19.20	1.07	0.91	0.85	1.07	0.91	0.85
S2	14.70	0.82	0.69	0.65	0.82	0.69	0.65
HEMATITE							
Particle	**D (nm)**	**Normalised Particle D**			**Normalised Particle D**		
H1	17.24	0.96	0.81	0.76	0.96	0.81	0.76
H2	15.83	0.88	0.75	0.70	0.88	0.75	0.70
H3	37.26	2.07	1.76	1.65	2.07	1.76	1.65

S.6 Molecular Dynamics

Geometry

Our MD setups were designed to be as close as possible to the experiments, within the computational limitations of MD. **Figure 2** in the main manuscript shows a snapshot of the MD case setup for the BNNT membrane. Both types of nanotubes of diameter D_P = 40.68 Å and length L = 20.40 Å used a pristine hexagonal structure and were embedded within a membrane surface of the same material. The nanotube length was kept short to reduce computational cost, as our interest lies in the particle dynamics at the pore entrance. The diameter was made as large as possible to ensure predominant bulk-like fluid in the nanotube [27].

Two reservoirs were filled with water and placed on either end of the nanotube membrane. The solvent (left) reservoir has dimensions $60 \times 81.1 \times 80.9$ Å, while the permeate (right) reservoir is $40 \times 81.1 \times 80.9$ Å; water of density 1000 kg m^{-3} was initialised in each reservoir and the nanotube pore. The left reservoir was purposely made much larger than the right to allow unimpeded Brownian motion of the particle, and allow enough time to take measurements (~8 ns) as water depleted from the left reservoir during steady flow conditions. Pistons on either side of the membrane maintained steady pressures (permeate side was always set at 1 bar). Various pressures were set to the solvent side: 5 bar, 20 bar, 60 bar, 100 bar and 1000 bar, in order to generate different pressure drops across the membrane. The force on each piston was transmitted to a rigid surface by setting the force on each atom to $F = p\,A/N$, where p is the applied pressure, A = 66 nm^2 is the area of the piston, and N = 2508 is the number of atoms on each piston. The direction of the force for the left piston was in the positive x direction, while the right piston was given a force in the negative x direction.

The particle was modelled as a hollow spherical shell made of one layer of rigid atoms distributed evenly across the sphere circumference. The *effective* diameter of the nanoparticles D_{NP}, were chosen in line with the experimental observations, i.e. slightly smaller than the nanotube diameter D_P such that $0.6 < D_{NP}/D_P < 1$, where D_{NP} includes the actual diameter of the nanoparticle and the water-particle intermolecular lengthscale $\sigma \approx$ 3 Å. Specifically, 5 cases were considered: D_{NP}/D_P = 1.0, 0.9, 0.8, 0.7, 0.6, which represent *actual* particle diameters of 32.544 Å, 28.476 Å, 24.408 Å, 20.34 and,16.272, respectively. All particles were initially placed 5 Å away from the pore, as measured between the entrance pore centre and the surface of the particle.

Force Fields

A hybrid pair-wise Lennard-Jones (LJ) and electrostatic Coulombic potentials were used for all atoms in the flow simulations:

$$U_{ij} = 4\epsilon_{ij}\left[\left(\frac{\sigma_{ij}}{r_{ij}}\right)^{12} - \left(\frac{\sigma_{ij}}{r_{ij}}\right)^{6}\right] + \frac{1}{4\pi\epsilon_0}\frac{q_i q_j}{r_{ij}}, \tag{S11}$$

where U_{ij} is the pair potential energy between atoms i and j, $\epsilon_{ij}$is the van der Waals interaction energy between a pair of interacting atoms (i,j), σ_{ij} is the characteristic length scale, r_{ij} is the distance between the atoms, q_i is the charge on atom i, and ϵ_0 is the vacuum permittivity.

The TIP4P/2005 model [28] along with the SHAKE algorithm [29] is used for modelling water molecules, which consist of two hydrogen (H) atoms (0.5564 e), one LJ oxygen (O) atom and one massless (M) site (-1.1128 e). The Coulombic interactions were modelled using the Particle-Particle Particle-Mesh (PPPM) method [30]. All short-range LJ interactions are shifted and truncated by a cut-off of 13.0 Å. The LJ parameters used for the interactions between all the atoms are given in Table S 10.

Table S 8 Lennard Jones force field parameters used in this work. No potential was applied between piston-piston, B-B, B-N, N-N, H-*ALL* and C-C pairs. [exp calib.] = calibrated from our experiments in this work; [est.] = estimated potential only required for transmitting pressure between piston and water; * the Si-O potential for particle-oxygen interactions is obtained from Lorentz-Berthelot mixing rules between O-O [28] and Si-Si [31] for σ, and calibration of ϵ from 20° experimentally-measured contact angle [32]; ** the Si-C particle-surface interactions were obtained from Lorentz-Berthelot mixing rules of Si-Si [31] and C-C [33].

Pair	ϵ **(kcal/mol)**	σ (Å)
O-O [3]	0.1852	3.159
O-B	0.0981 [exp calib.]	3.322 [7]
O-N	0.1213 [6]	3.278 [7]
O-Particle*	0.1912	3.433
O-Piston [est.]	0.3000	3.000
B/N/C-Particle**	0.0004	3.706
C-O [8]	0.1020	3.190

The surface partial charges of the BNNT and CNT were determined using charge equilibration in LAMMPS using the $\text{ReaxFF}_{\text{HBN}}$ force field [34]; this produced an equilibrated nanotube structure with a net neutral charge on the surface. The boron atoms on average were found to have a 0.9 *e* charge, nitrogen atoms a -0.9 *e* charge, and no charge for carbon atoms on the CNT.

Oxygen-boron, oxygen-nitrogen and oxygen-carbon potentials (see Table S 10) were obtained using calibration studies with our experiments of water droplet contact angle measurements on surfaces of the same materials as the membranes, a method we describe in [5]. For BN surfaces we used a macroscopic contact angle of 78°, while for graphene we use 86°.

We modelled the zeta potential of the hydrated surfaces to be equal to that measured near the membranes in the experiments by subtracting charges from the boron atoms to produce a semi-hydrogenated surface with an overall negative surface charge density of -1.28e-20 C nm^{-2}, which resulted in a change of -0.005 *e* per atom. The zeta potential near the CNT surface was found to be close to zero so no changes were applied to the partial charges. The particle charge density was set to -6.99x10^{-21} C nm^{-2} (also measured from experiments), which resulted in -0.003 *e* per atom.

MD simulations

An NVT MD ensemble was adopted in all flow cases, using the velocity Verlet algorithm with an integration time-step of 2 fs. A streamwise-velocity unbiased Berendsen thermostat was used to maintain the temperature of the water at 300 K for the duration of the simulation. After initialising the cases as discussed above, an equilibration simulation was run to allow the pistons to set the target pressures in their respective reservoirs, while the particle was kept rigid, until a steady flow was generated (~ 0.5 ns). After this equilibration period, the particle was released and the production MD simulations were run for around 8 ns, during which all Lagrangian data was output every 1000 timesteps for further post-processing.

All our simulations were run on the UK's National Supercomputer Facility (ARCHER), using 96 processors for each case.

Results

The measurement of mass flow rate represents a way of probing the loss in pressure created by the impeding particle at the pore entrance. The flow rate was estimated by considering the total number of water molecules in the left and right reservoirs of Figure 2 and fitting a straight line through their variation with time, as shown in Figure S15 a and b for BNNT and CNT, respectively.

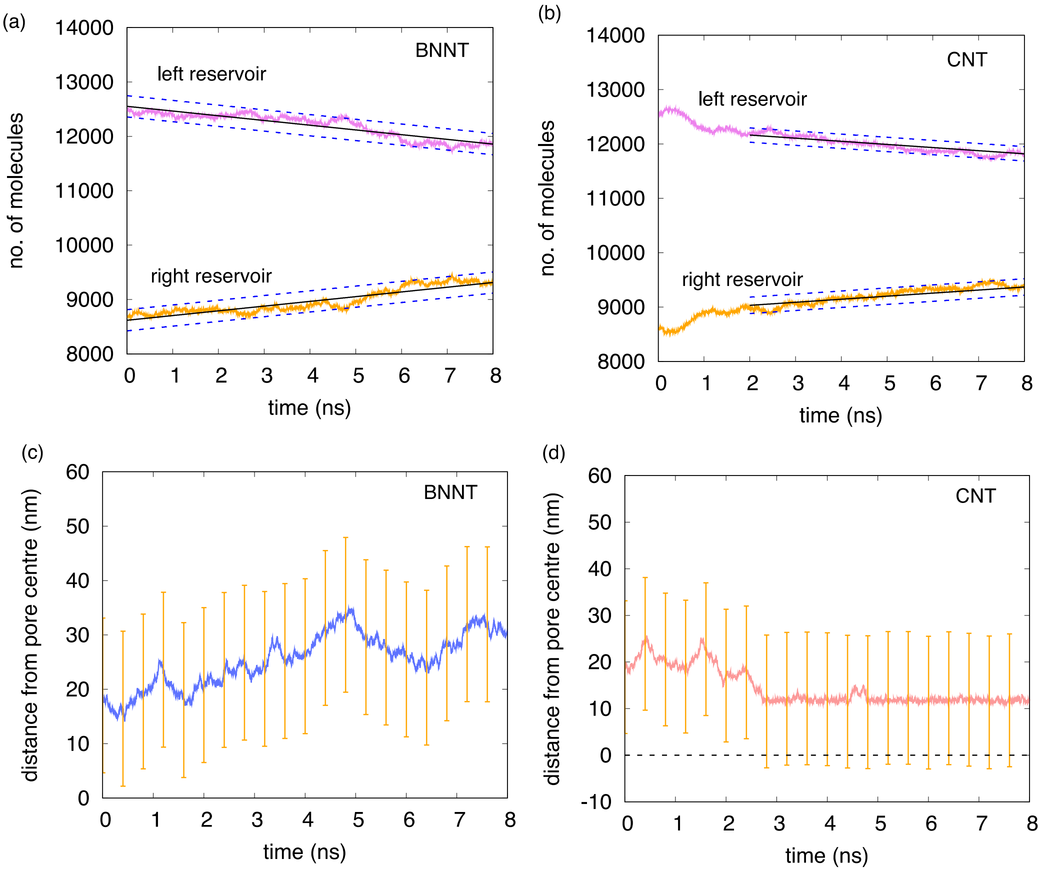

Figure S15 (a), **(b)** the number of molecules in the left and right reservoir as a function of time leads to the mass flow rate measurement; **(c) (d)** magnitude distance of particle from pore centre. In the top figures, black solid lines indicate fit through data, from which flow rate is the gradient of this line multiplied by the mass of one water molecule, while blue dotted lines indicate the uncertainty in the prediction. In the bottom figures, yellow vertical lines indicate the diameter of the particle (28.5 nm).

Figure S 16 shows the flow rate with increasing pressure for three D_{NP}/D_P ratios. We also compare the results with benchmark cases, which are similar simulations, but which not include the particle. In these benchmark cases, we similarly measure flow rate for increasing pressure and fit a line of best fit of the form $\Delta p = R\,\dot{m}$, where R is the gradient. For unimpeded particle flow, the CNT enables more water transport than the BNNT, which is understood due to the lower nanotube friction and slip length. For the pristine CNT, the measured slip length is 50 nm, while for the pristine BNNT the slip length is 13 nm. In previous work we found that defects decrease the slip length substantially, so we expect these values to be a maximum and larger than those seen in experiments [5, 35]. Given the length of the tubes in the experiments, we expect the pressure loss over the membrane to be dominant in the tube [5], so it is possible to predict the flow through the tube using the Hagen Poiseuille flow equation with slip, with slip lengths as mentioned above.

As expected, for the particle-impeded flow the transport is seen to drop below the benchmark for all cases because the particle blocks the mouth of the pore. We find that the drop in flow rate for the BNNT seems to be lower than that for the CNT. For example, for $D_{NP}/D_P \sim 0.9$ at pressure drop of 2 MPa, the drop in the flow rate is 13% for the BNNT and 40% for CNT, and at 6 MPa, the drop is 40% for BNNT and 70% for CNT. The reason for this difference in performance between BNNT and CNT lies in the positioning of the particle. In the BNNT, the particle is pushed further away from the pore due to the stronger interatomic charges, as we show in Figure S 16d of the main paper. Figure S 17 shows that below ~4 MPa, the particle ($D_{NP}/D_P \sim 0.9$) near the BNNT is still mobile, and has the tendency of moving back into the reservoir. For the CNT, the retreat of the particle back into the bulk is observed at lower pressures (i.e. < 2 MPa). Above 4 MPa of pressure, Figure S 17 shows both particles are lodged at the same distance away from the pore, and this is reflected in the further drop in flow rate by the BNNT. This observation lays the case for using BNNT surfaces for water filtration at pressures lower than 4 MPa; they are more likely to repel particles for this particle diameter ratio of $D_{NP}/D_P \sim 0.9$.

Evidence of differences in particle mobility are also measured using the Mean Squared Displacement [36], as shown in Figure S 18. For the low pressures (Figure S 18a), the particle near the BNNT is more mobile than the CNT. For larger pressures (Figure S 18b), the BNNT however is more constrained at the pore, which we think is due to the larger repulsion in the surface-particle forces.

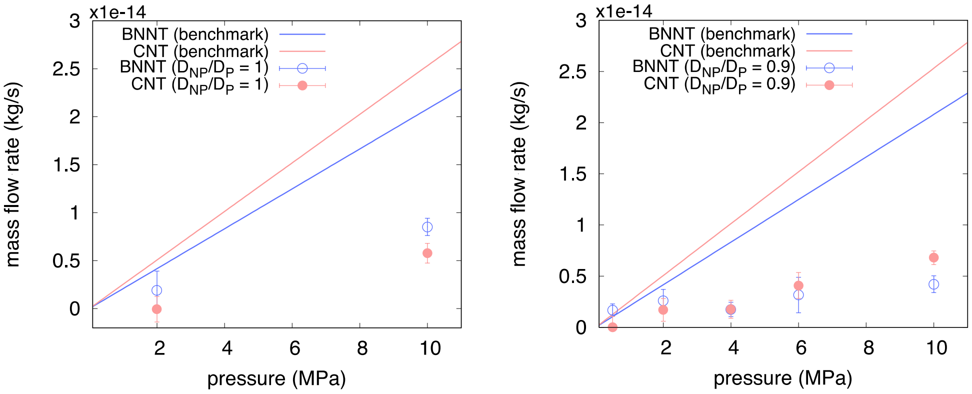

(a) $D_{NP}/D_P \sim 1.0$ (b) $D_{NP}/D_P \sim 0.9$

Figure S 16 Mass flow rates against pressure drop for BNNT and CNT cases, and two D_{NP}/D_P ratios **(a)** 1.0 and **(b)** 0.9.

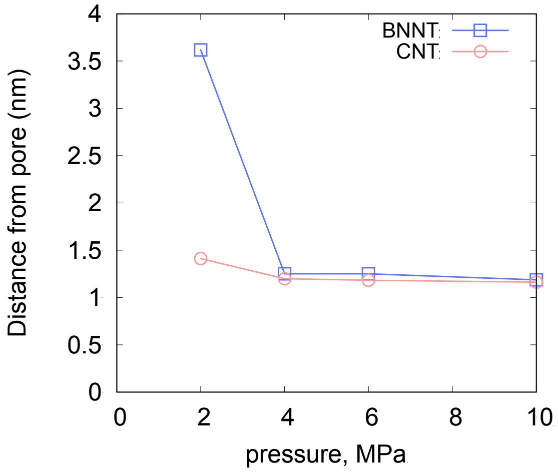

Figure S 17 Distance between pore and particle against applied pressure for BNNT/CNT; $D_{NP}/D_P = 0.9$.

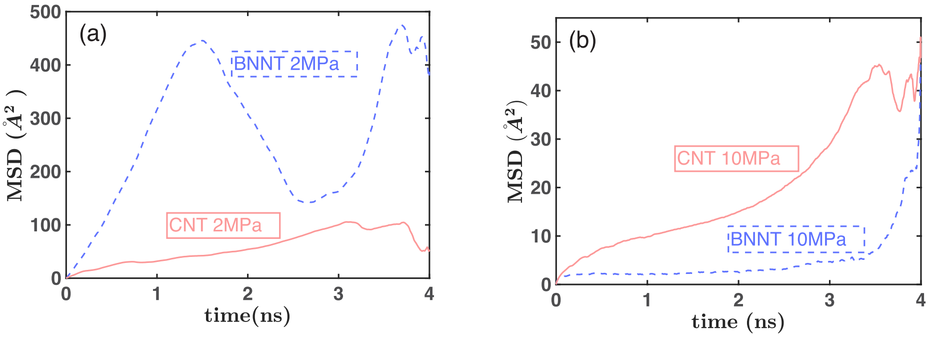

Figure S 18 MSD plots for D_{NP}/D_P ~0.9 for **(a)** 2MPa and **(b)** 10MPa.

In order to investigate the equilibrium position of particles near the mouth of the BNNT and CNT membranes, and therefore get an idea of probability of selection, we conduct a second independent set of MD simulations. Here the particles are displaced radially and axially to the pore at small increments; at each position the particle is frozen, and a pressure drop simulation of 20 bar was applied. In all cases, flow was allowed to reach a steady state around the fixed particle, before measurements are taken. We then determine the force balance on the particle due to intermolecular interactions between particle-membrane and particle-water.

The individual force contributions on the particle from the water and the wall atoms were calculated by switching off the unwanted interactions and recalculating the forces based on the position data. We measured the *particle-water* forces Δf_P and the *particle-surface* forces Δf_C. In our particle simulations we find that the particle-surface force has low noise (which makes sense), while particle-water forces has large thermal noise, indicating the dominant Brownian force component. We have produced graphs of distribution of the water-particles forces and have found the mean force (**Figure S 19**). We compared these to the particle-surface forces. The particle-water forces are normally distributed, while the particle-surface force has a near constant value. When a particle is at a pore, and there is a steady flow, the mean of the forces balance out to almost zero. This is expected.

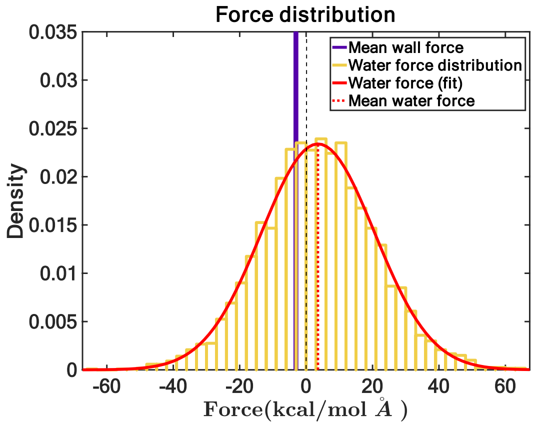

Figure S 19 Distribution of forces on nanoparticle for D_{NP}/D_P ~0.9, BNNT membrane.

To produce contour plots of $\Delta f = \Delta f_C - \Delta f_P = 0$ vs D_{NP}/D_P (Fig. S20) we ran simulations with the particles at fixed locations, and measure particle-water and particle-surface charges at those locations. This allows us to build a contour plot for Δf. The particle-liquid force which we measure is equal to dFP. The negative value of df indicates repulsion from the pore, while a positive value indicates attraction.

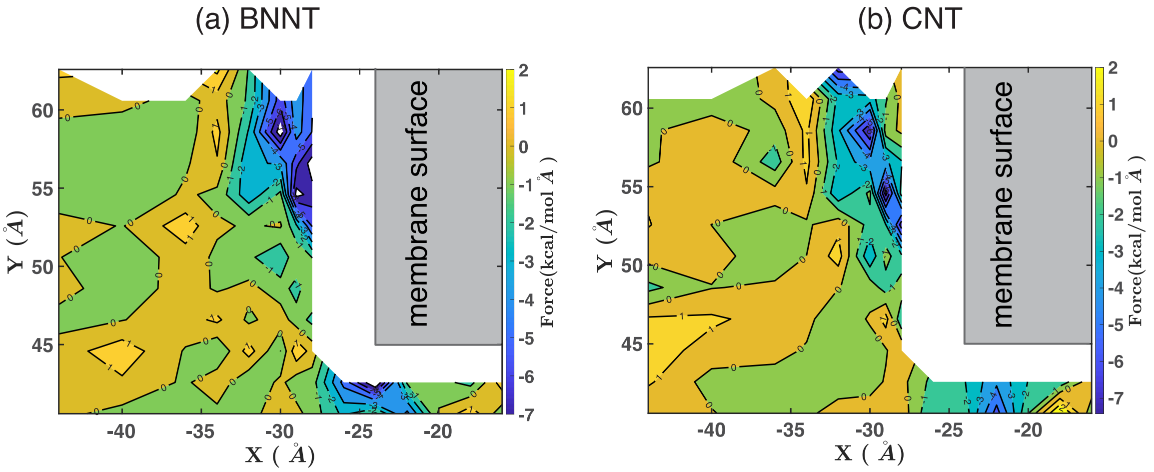

Figure S 20 Contour plots for Δf for $D_{NP}/D_P \sim 0.9$, $\Delta p = 20$ bar: **(a)** BNNT and **(b)** CNT; The membrane surface has been displaced by the particle radius (14.2 nm) in these figures for better clarity.

The plots for $\Delta f = 0$ (Fig. S21), extracted from the contour plots for Δf show that while smaller D_{NP}/D_P experience zero force at almost similar locations, this is not true for the larger values of D_{NP}/D_P, where the BNNT pushes the particle further away from the pore due to surface charges. This transition happens about $D_{NP}/D_P \sim 0.8$. This is due to the increasing contribution of the electrostatic repulsion as the particle size increases, creating a difference between the forces experienced due to the charge carrying BNNT surface and the uncharged CNT surface.

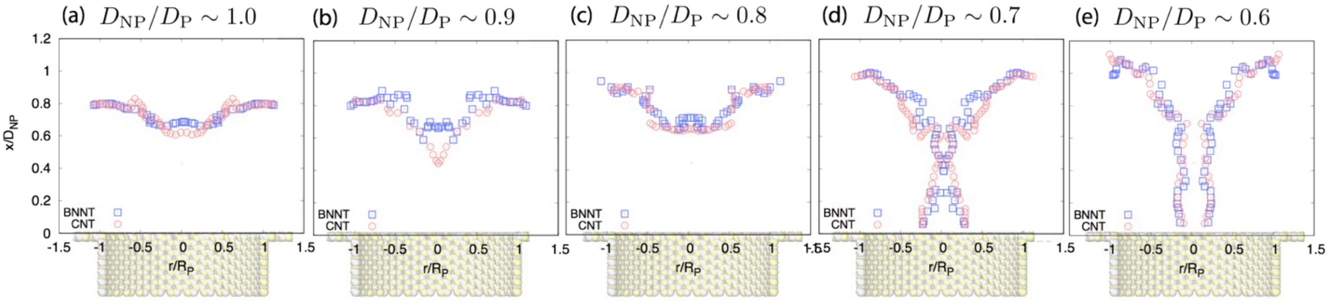

Figure S 21 Iso-force graphs for BNNT/CNT membranes with particle/pore diameter ratios $0.6 < D_{NP}/D_P < 1$ and applied pressure drop $\Delta p = 20$ bar.

The MD results for three of the investigated ratios are reported in Figure 3c of this work and are displayed in Figure S 22.

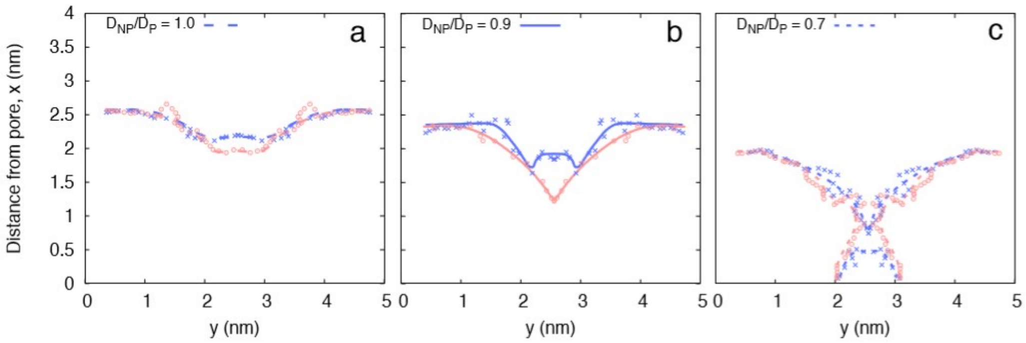

Figure S 22 MD data for selected ratios displayed in Figure 3c.

References

1. Kim, G.; Jang, A.-R.; Jeong, H. Y.; Lee, Z.; Kang, D. J.; Shin, H. S., Growth of high-crystalline, single-layer hexagonal boron nitride on recyclable platinum foil. *Nano letters* **2013,** *13* (4), 1834-1839.
2. Jessensky, O.; Müller, F.; Gösele, U., Self-organized formation of hexagonal pore arrays in anodic alumina. *Applied physics letters* **1998,** *72* (10), 1173-1175.
3. Mattia, D.; Leese, H.; Lee, K. P., Carbon nanotube membranes: from flow enhancement to permeability. *Journal of Membrane Science* **2015,** *475*, 266-272.
4. Mattia, D.; Rossi, M.; Kim, B.; Korneva, G.; Bau, H.; Gogotsi, Y., Effect of graphitization on the wettability and electrical conductivity of CVD-carbon nanotubes and films. *The Journal of Physical Chemistry B* **2006,** *110* (20), 9850-9855.
5. Casanova, S.; Borg, M. K.; Chew, Y. J.; Mattia, D., Surface-controlled water flow in nanotube membranes. *ACS applied materials & interfaces* **2018,** *11* (1), 1689-1698.
6. Low, Z.-X.; Ji, J.; Blumenstock, D.; Chew, Y.-M.; Wolverson, D.; Mattia, D., Fouling resistant 2D boron nitride nanosheet – PES nanofiltration membranes. *Journal of Membrane Science* **2018,** *563*, 949-956.
7. Barwick, V. *Preparation of Calibration Curves*; 2003.
8. Barwick, V. J. Preparation of calibration curves: A guide to best practice. https://www.lgcgroup.com/our-science/national-measurement-laboratory/publications-and-resources/good-practice-guides/preparation-of-calibration-curves-a-guide-to-best/#.W3c6XiDTW5s.
9. Wenzel, R. N., Surface roughness and contact angle. *The Journal of Physical Chemistry* **1949,** *53* (9), 1466-1467.
10. Mulder, J., *Basic principles of membrane technology*. Springer Science & Business Media: 2012.
11. Lin, T.; Zhang, J.; Chen, W., Recycling of activated carbon filter backwash water using ultrafiltration: Membrane fouling caused by different dominant interfacial forces. *Journal of Membrane Science* **2017,** *544*, 174-185.

12. Kim, M.-m.; Zydney, A. L., Effect of electrostatic, hydrodynamic, and Brownian forces on particle trajectories and sieving in normal flow filtration. *Journal of Colloid and Interface Science* **2004,** *269* (2), 425-431.

13. Ermak, D. L.; Buckholz, H., Numerical integration of the Langevin equation: Monte Carlo simulation. *Journal of Computational Physics* **1980,** *35* (2), 169-182.

14. Bowen, W. R.; Filippov, A. N.; Sharif, A. O.; Starov, V. M., A model of the interaction between a charged particle and a pore in a charged membrane surface. *Advances in Colloid and Interface Science* **1999,** *81* (1), 35-72.

15. Li, A.; Ahmadi, G., Dispersion and deposition of spherical particles from point sources in a turbulent channel flow. *Aerosol science and technology* **1992,** *16* (4), 209-226.

16. Li, H.; Zeng, X. C., Wetting and interfacial properties of water nanodroplets in contact with graphene and monolayer boron–nitride sheets. *ACS nano* **2012,** *6* (3), 2401-2409.

17. Megias-Alguacil, D.; Tervoort, E.; Cattin, C.; Gauckler, L. J., Contact angle and adsorption behavior of carboxylic acids on α-Al2O3 surfaces. *Journal of colloid and interface science* **2011,** *353* (2), 512-518.

18. Lee, K. P.; Leese, H.; Mattia, D., Water flow enhancement in hydrophilic nanochannels. *Nanoscale* **2012,** *4* (8), 2621-7.

19. Baroña, G. N. B.; Lim, J.; Choi, M.; Jung, B., Interfacial polymerization of polyamide-aluminosilicate SWNT nanocomposite membranes for reverse osmosis. *Desalination* **2013,** *325*, 138-147.

20. Bresnehan, M. S.; Hollander, M. J.; Wetherington, M.; Wang, K.; Miyagi, T.; Pastir, G.; Snyder, D. W.; Gengler, J. J.; Voevodin, A. A.; Mitchel, W. C., Prospects of direct growth boron nitride films as substrates for graphene electronics. *Journal of Materials Research* **2014,** *29* (3), 459-471.

21. Lee, K. P.; Mattia, D., Monolithic nanoporous alumina membranes for ultrafiltration applications: Characterization, selectivity–permeability analysis and fouling studies. *Journal of membrane science* **2013,** *435*, 52-61.

22. Weber, M.; Koonkaew, B.; Balme, S.; Utke, I.; Picaud, F.; Iatsunskyi, I.; Coy, E.; Miele, P.; Bechelany, M., Boron nitride nanoporous membranes with high surface charge by atomic layer deposition. *ACS applied materials & interfaces* **2017,** *9* (19), 16669-16678.

23. Lei, W.; Mochalin, V. N.; Liu, D.; Qin, S.; Gogotsi, Y.; Chen, Y., Boron nitride colloidal solutions, ultralight aerogels and freestanding membranes through one-step exfoliation and functionalization. *Nature communications* **2015,** *6*, 8849.

24. Sprycha, R., Electrical double layer at alumina/electrolyte interface: I. Surface charge and zeta potential. *Journal of Colloid and Interface Science* **1989,** *127* (1), 1-11.

25. Secchi, E.; Marbach, S.; Niguès, A.; Stein, D.; Siria, A.; Bocquet, L., Massive radius-dependent flow slippage in carbon nanotubes. *Nature* **2016,** *537* (7619), 210-213.

26. Plimpton, S., Fast parallel algorithms for short-range molecular dynamics. *Journal of computational physics* **1995,** *117* (1), 1-19.

27. Borg, M. K.; Lockerby, D. A.; Ritos, K.; Reese, J. M., Multiscale simulation of water flow through laboratory-scale nanotube membranes. *Journal of Membrane Science* **2018,** *567*, 115-126.

28. Abascal, J. L.; Vega, C., A general purpose model for the condensed phases of water: TIP4P/2005. *The Journal of chemical physics* **2005,** *123* (23), 234505.

29. Ryckaert, J.-P.; Ciccotti, G.; Berendsen, H. J., Numerical integration of the cartesian equations of motion of a system with constraints: molecular dynamics of n-alkanes. *Journal of computational physics* **1977,** *23* (3), 327-341.

30. Hockney, R. W.; Eastwood, J. W., *Computer simulation using particles*. crc Press: 1988.

31. Cygan, R. T.; Liang, J.-J.; Kalinichev, A. G., Molecular models of hydroxide, oxyhydroxide, and clay phases and the development of a general force field. *The Journal of Physical Chemistry B* **2004,** *108* (4), 1255-1266.
32. Zambrano, H.; Walther, J. H.; Jaffe, R., Molecular dynamics simulations of water on a hydrophilic silica surface at high air pressures. *Journal of Molecular Liquids* **2014,** *198*, 107-113.
33. Walther, J. H.; Jaffe, R. L.; Kotsalis, E.; Werder, T.; Halicioglu, T.; Koumoutsakos, P., Hydrophobic hydration of C60 and carbon nanotubes in water. *Carbon* **2004,** *42* (5-6), 1185-1194.
34. Han, S. S.; Kang, J. K.; Lee, H. M.; Van Duin, A. C.; Goddard III, W. A., The theoretical study on interaction of hydrogen with single-walled boron nitride nanotubes. I. The reactive force field ReaxFF HBN development. *The Journal of chemical physics* **2005,** *123* (11), 114703.
35. Nicholls, W.; Borg, M. K.; Lockerby, D. A.; Reese, J., Water transport through carbon nanotubes with defects. *Molecular Simulation* **2012,** *38* (10), 781-785.
36. Tarantino, N.; Tinevez, J.-Y.; Crowell, E. F.; Boisson, B.; Henriques, R.; Mhlanga, M.; Agou, F.; Israël, A.; Laplantine, E., TNF and IL-1 exhibit distinct ubiquitin requirements for inducing NEMO–IKK supramolecular structures. *J Cell Biol* **2014,** *204* (2), 231-245.